Title: Functional recovery of adult brain tissue arrested in time during cryopreservation by vitrification

Authors: Alexander German[1]*, Enes Yağız Akdaş[2], Cassandra Flügel-Koch[3], Anna Fejtova[2], Jürgen Winkler[1], Christian Alzheimer[4], Fang Zheng[4]

Affiliations:

[1]Department of Molecular Neurology, Universitätsklinikum Erlangen, Friedrich-Alexander-Universität Erlangen-Nürnberg, Erlangen, Germany

[2]Department of Psychiatry and Psychotherapy, Universitätsklinikum Erlangen, Friedrich-Alexander-Universität Erlangen-Nürnberg, Erlangen, Germany

[3]Institute of Functional and Clinical Anatomy, Friedrich-Alexander-Universität Erlangen-Nürnberg, Erlangen, Germany

[4]Institute of Physiology and Pathophysiology, Friedrich-Alexander-Universität Erlangen-Nürnberg, Erlangen, Germany

*Corresponding author. Email: alex.german@fau.de

Abstract: Cryopreserving adult brain tissue is challenging due to damage from ice formation, and traditional freezing methods fail to maintain neural architecture and function. Vitrification offers a promising alternative but has not been surveyed in the brain. Here, we demonstrate near-physiological recovery of adult mouse hippocampal slices after vitrification. Key features of this cognitive hub are preserved, including structural integrity, metabolic responsiveness, neuronal excitability, and synaptic transmission and plasticity. Notably, hippocampal long-term potentiation was well preserved, indicating that the cellular machinery of learning and memory remains operational. These findings extend the knowledge of brain recovery after hypothermic shutdown to recovery after complete cessation of molecular mobility through vitrification. This suggests that brain tissue can be arrested in time and reactivated, opening avenues for potential clinical applications.

Main Text:

Bridging space and time via suspended animation is a familiar theme from fiction (*1, 2*), and it has found short-term application through procedures like deep hypothermic circulatory arrest (DHCA (*3*)). The brain's remarkable capacity to recover from hypothermic shutdown demonstrates the potential to re-initialize brain dynamics (*4*), and supports the tenet that memory is structurally encoded in the synaptic architecture, a fundamental assumption in connectomics (*5*). However, it is not known whether brain function can be restored after complete shutdown of molecular mobility. Here, we establish near-physiological functional recovery after cryopreservation by vitrification of adult mouse brain tissue. This holds immediate promise: For example, it allows the distribution of neuroscientific experiments across space and time, improving reproducibility and animal welfare (*6*). Furthermore, cryosubstitution of vitrified samples enables structural analysis in a near-native state, e.g., for connectomics (*7, 8*). Progress in cryopreservation of rodent organs has moved the theme of long-term suspended animation closer to plausibility (*9-13*), with the nervous system remaining as a cornerstone on the path towards clinical applications (*14, 15*). Finally, empirical proof that brain function can be arrested in time could inform philosophical debates, e.g., whether mental phenomena resist physical explanation (*16-18*).

Already in 1953, Luyet and Gonzales demonstrated the possibility to cryopreserve embryonic avian brain tissue (*19*), and cellular survival after cryopreservation by freezing was later also shown for fetal rodent and human brain tissue (*20-23*). In the case of adult mammalian brain tissue and neurons differentiated in culture, full electrophysiological recovery after cryopreservation has thus far not succeeded (*24-26*). Using freezing techniques, some recovery of activity was reported in the adult feline brain after several years of storage at -20 °C (*27, 28*), and in rodent ganglia after up to 24 hours storage at -76 °C (*29*), both using 15% glycerol. Xue et al. showed recovery of neural organoids after freezing, using 10% dimethyl sulfoxide and 10% ethylene glycol combined with a ROCK-inhibitor (*30*). However, freezing of neural tissue results in overt loss of synaptic connections (*31, 32*). Achieving full electrophysiological recovery therefore likely requires ice-free cryopreservation, i.e., vitrification.

During cryopreservation by vitrification, the aqueous phase of biological tissue solidifies into a non-crystalline amorphous glass (*33, 34*). This can be achieved by replacing high proportions of the tissue water with polar solvents. Provided sufficient cooling and rewarming rates, these solvents act as cryoprotectants, inhibiting crystallization due to water-water interactions (*35*). Ice-free cryopreservation to avoid mechanical disruption of the inter- and intracellular space in complex biological materials has been proposed long ago (*36, 37*), and has been realized by vitrification (*33, 38*). Recent progress in rapid and uniform warming techniques has finally enabled cryopreservation by vitrification of the rat heart (*10*), liver (*11*) and kidney (*9, 12, 13*).

Pichugin et al. have demonstrated recovery of K^+/Na^+ ratios after vitrification of rat hippocampal slices at -130 °C (*32*). Based on this finding, we vitrified mouse brain slices using a variant of the vitrification solution VM3 which we call V3 (*39*), containing a mixture of dimethyl sulfoxide, formamide and ethylene glycol. We held the slices below the glass transition temperature at -196 °C, ensuring complete cessation of molecular mobility. With an optimized vitrification procedure, we were able to achieve recovery of cellular metabolism and electrophysiology by patch-clamp recordings, and extracellular field postsynaptic potentials (fPSPs) including short-term and long-term synaptic plasticity. This establishes a bona fide method to preserve functional brain tissue.

An optimized vitrification protocol

Based on stereomicroscopy assessment of tissue swelling and crystallization, as well as the degree of electrophysiological recovery, we optimized a vitrification procedure that minimizes damage from the following six variables (*35, 39*): 1. Toxicity of cryoprotective agents (CPA), determined by their composition, concentration, temperature and exposure time before vitrification and after rewarming (*39*). 2. Osmotic shrinking determined by the CPA loading protocol before vitrification (*40-42*). 3. Osmotic swelling determined by the CPA unloading protocol after rewarming (*40-42*). 4. Crystallization determined by the CPA concentration, composition, diffusion, and the rate of cooling for vitrification and the rate of rewarming (*33*). 5. Physical cracking determined by thermomechanical stress during cooling and rewarming in the vitreous state (*43*). 6. Chilling injury determined by temperature and exposure time before vitrification and after rewarming (*44*).

Fig. 1A illustrates our optimized vitrification procedure for adult mouse brain slices. Slices were put on a polyester mesh insert, and went through a protocol starting with CPA loading in LM5 carrier solution (**table S1**) containing 0%, 2%, 4%, 8%, 16% and 30% w/v vitrification solution V3 (**table S2**) at 10 °C. This was followed by 45% w/v V3 and three iterations of 59% w/v V3 at -10 °C. Reliability was increased by precise preparation of V3 using a volumetric flask and by consistently submerging the brain slices into the above solutions with a brush. Brain slices were directionally cooled from below, by placing them on a copper cylinder cooled to -196 °C with liquid nitrogen (**fig. S1**). The mesh insert carrying the slices was first transferred onto the top of the cylinder. After one minute, the mesh insert was slowly transferred into liquid nitrogen. This allowed us to avoid physical cracking of vitreous brain slices due to thermomechanical stress, as would occur during direct immersion into liquid nitrogen (**fig. S2**).

We varied the final loading of CPA (at -10 °C) with concentrations ranging from 45% to 65% w/v V3, as tissue vitrification properties are tissue dependent and empirical (*45*). During cooling and rewarming, successful cryopreservation was predictable by direct visual observation, with vitreous slices staying glossy and transparent (**Fig. 1B**). Failure of cryopreservation was predictable when slices turned dull and opaque, due to apparent cooling phase crystallization (**Fig. 1B**) and/or transient rewarming phase crystallization ((*46*), **fig. S3, Movie S1-S7**). Using the stereomicroscope, we observed complete avoidance of cooling phase crystallization with CPA concentrations starting from 58%. Complete avoidance of transient rewarming phase crystallization was observed starting from 56% w/v V3 when using rapid rewarming (**Movie S8-S11**). Successful recovery after cryopreservation was achieved starting from 57% w/v V3. We observed complete avoidance of rewarming phase crystallization with 65% w/v V3 even during slow rewarming (**fig. S4**, **Movie S12**). The determining factor for brain slice vitrification in the final CPA loading step was therefore cooling phase crystallization. If not otherwise specified, for all presented analyses, a standard concentration of 59% w/v V3 was used to ensure complete avoidance of ice formation when using rapid rewarming.

After 10 min to 7 days in liquid nitrogen and then in a -150 °C freezer, slices were rewarmed in 52% V3 at -10 °C. CPA unloading was performed in LM5 with additional 300 mM mannitol to reduce osmotic swelling. The solutions used were 45% and 30% w/v V3 at -10 °C, 16%, 8%, 4%, 2%, 0% w/v V3 at 10 °C. Unloading was concluded with a final step of LM5 without added mannitol (**Fig. 1A, table S3**).

Our optimized protocol balances damage from osmotic changes of cell volume due to transmembrane solute-solvent flux during concentration changes of CPA with the temperature-

and time-dependent toxicity of higher CPA concentrations (*40, 41*). Limited cell shrinking and swelling can be beneficial to minimize intracellular exposure to peak CPA concentrations (*38, 42*). We varied concentration and timing of CPA loading and unloading steps. For example, all slices incubated in concentrations of 30% w/v V3 and above showed a transient swelling (8% increase in area) with faint whitening and loss of transparency during CPA unloading (**fig. S5**). This swelling appeared at 16% w/v V3 concentration at 10 °C and became more pronounced during incubation in decreasing concentration steps. It disappeared after 15 minutes of post-incubation in artificial cerebrospinal fluid (aCSF) at room temperature (RT). This transient swelling could be mitigated by extending the incubation time in 16% w/v V3 during unloading, improving subsequent electrophysiological recovery. Introducing an intermediate step of 45% w/v V3 during loading and unloading increased the yield of superficial neurons in subsequent patch-clamp recordings.

Metabolic and morphologic recovery of vitrified brain tissue

Mitochondrial activity of brain slices was evaluated in the CA1 region based on oxygen consumption rate (OCR, measured in pmol/min). Using the optimized protocol, slices were loaded up to different peak CPA concentrations, subsequently unloaded and incubated for two hours in aCSF at room temperature (RT) for recovery. Vitrification was omitted. Peak CPA concentrations where: low (30% w/v V3 equivalent to 4.28 M permeable CPA, n = 7), standard (59% w/v V3 equivalent to 8.42 M permeable CPA, n = 6) and high (65% w/v V3 equivalent to 9.28 M permeable CPA, n = 5). These were compared to fresh tissue (n=8) and vitrification with standard CPA concentration (n = 8) (**Fig. 1C**). CPA exposure reduced the basal respiration (control: 173.3±6.7, low CPA: 139.7±3.1, standard CPA: 135.1±6.7, high CPA: 80.4±5.6, Spearman's r = −0.9018, permutation-based p = 0.0002). We did not observe a change between standard CPA and vitrification (standard CPA: 135.1±6.7, vitrification: 131.4±5.7). Higher concentrations of CPA significantly reduced the spare capacity (control: 73.4±5.7, low CPA: 62.3±8.0, standard CPA: 48.6±5.8, high CPA: 38.9±5.6, Spearman's r = −0.6731, permutation-based p = 0.0004). Again, we did not observe a change between standard CPA and vitrification (standard CPA: 48.6±5.8, vitrification: 50.6±6.4).

Metabolic analysis therefore showed slightly reduced basal respiration after 30% w/v and 59% CPA loading, and markedly reduced rates after exposure to 65% w/v V3 solution to about half of control values. This sharply increasing toxicity of CPA was also manifested in the maximal respiratory capacity (**Fig. 1C**).

Light and electron microscopic analyses were further employed to evaluate the potential morphological changes after standard CPA loading and vitrification. Nissl staining of brain sections (30 µm) revealed overall normal morphology after vitrification (n = 6 for 1-5 hours), compared to control untreated slices (**Fig. 1D)**. Electron microscopy of ultrathin sections (50 nm; **Fig. 1E**) indicated clear neuronal and synaptic structures in the hippocampus. Fixation performed immediately after completion of CPA unloading revealed limited mitochondrial swelling (**Fig. 1E(i)**). Like macroscopic swelling (**fig. S5**), this ultrastructural swelling of this organelle resolved during incubation in aCSF at RT and was not observed in slices incubated for 1-10 hours after rewarming, which exhibited regular ultrastructure like untreated controls (n=4 for 1-10 hours, **Fig. 1E(ii)-(iv)**).

Electrophysiological recovery of vitrified brain tissue

Next, we interrogated the functionality of the hippocampal circuitry after cryopreservation by vitrification with standard CPA concentration (59% w/v V3), focusing first on the Schaffer

collateral (SC) - CA1 pyramidal cell synapse, arguably the best studied synapse in the mammalian brain. Combined with extracellular recording in CA1 stratum radiatum, electrical stimulation of SC evoked field postsynaptic potentials (fPSPs, **Fig. 2)** predominantly mediated by AMPA-type glutamate receptors, as indicated by their sensitivity to CNQX (40 µM; **fig. S6A**). When comparing untreated slices (n = 9) with vitrified slices (n = 23), the input-output (I-O) curve from the latter preparation showed a trend towards a lower gain in fPSP amplitude with increasing stimulus intensities (50 - 200 µA), leading to a downward deflection of the curve, which reached significance at the maximum response (**Fig. 2A**). Loading with 59% w/v alone produced an I-O curve that was situated in between the curves from untreated and vitrified slices (**Fig. 2A**, blue curve), without being significantly different from untreated controls. This finding suggests that, despite the known dose-dependent toxicity of CPA (*39*), the standard concentration used here for vitrification did not inflict appreciable damage upon basic synaptic properties. Note that even after loading with a substantially lower CPA concentration (30% w/v), the I-O curve tended to level off at high stimulus intensity (**fig. S6B**).

Like many other excitatory synapses in the brain, the SC-CA1 synapse exhibits a rich repertoire of brief changes and persistent alterations, critically depending on the particular kind of input pattern. Whereas short-term plasticity (STP) involves mainly presynaptic mechanisms, long-term plasticity relies heavily on the postsynaptic machinery. We probed STP using a brief stimulus train (5 pulses at 20 Hz), with the stimulus intensity set to about 35% of that evoking the maximum response. We observed frequency facilitation in all groups (**Fig. 2B**). For the analysis, fPSP responses to 2nd – 5th stimuli were normalized to 1st stimulus in the train. STP was significantly attenuated in vitrified slices, whereas loading alone did not alter the extent of STP measured in untreated slices (**Fig. 2B**). To exclude that an overall decrease in the transmitter pools that can be released and mobilized accounts for reduced STP after vitrification, we used the K^+ channel blocker 4-aminopyridine (4-AP, 50 µM) to achieve maximum transmitter release from the terminals. When we plotted the gradual increase in fPSP amplitude as 4-AP was washed into the slice, neither the time course of drug action nor the maximum response that was eventually attained differed between the three groups (**Fig. 2C**).

We then examined long-term potentiation (LTP), the most important form of lasting plasticity and widely recognized as a key neurobiological substrate of learning and memory formation. Attesting to the astonishing tolerability of vitrification, cryopreserved hippocampal slices reliably produced LTP, which we induced using a standard protocol of high frequency stimulation (HFS, 100 Hz for 1 s, delivered twice 20 s apart **Figs. 2D-F**). Although the trajectories of potentiation tended to be different, in quantification over 51-60 min post-HFS, SC-CA1 LTP amounted to 160.50 ± 8.95 % in untreated slices (n = 7), which was not significantly different from the extent of LTP in vitrified slices (138.06 ± 6.90 %, n = 7; p = 0.070). To add weight to the striking finding of operational LTP post-vitrification, we extended our study to another essential synapse within the hippocampal formation that gates and processes incoming signals from the neocortex. This synapse is formed by the medial perforant path (mPP) of entorhinal cortex origin projecting onto granule cells (GC) of the dentate gyrus. Compared to untreated controls, the mPP-GC synapse in vitrified slices showed a significant downward shift of the I-O curve, especially across lower stimulation intensities (**fig. S6C,** left). However, STP and LTP of mPP-GC synapses were indistinguishable between the two groups, indicating full recovery of both transient and persistent synaptic plasticity after vitrification (**fig. S6C,** right**; Fig. 2F**)

To examine the effects of cryopreservation on cellular excitability, we performed whole-cell recordings from CA1 pyramidal cells (PCs) and dentate gyrus GCs in control and vitrified brain slices (with 59% w/v CPA) containing the dorsal hippocampus. Some cryopreserved cells were filled with biocytin to demonstrate the characteristic morphology with soma, apical and basal dendrites (**Fig. 3A**). In current-clamp mode, vitrified CA1 PCs had a resting membrane potential (RMP) of -74.82 ± 1.12 mV (n = 13), which was virtually identical to that of untreated cells (-74.65 ± 0.73 mV; n = 21, p = 0.779). The same was true for membrane capacitance (C_m) and input resistance (R_m) (**fig. S7A-C**). In contrast, vitrified GCs in dentate gyrus exhibited a small but significant depolarization of their RMP (vitrified-GC -83.53 ± 1.24 mV, n = 16; control-GC -86.00 ± 0.45 mV, n = 29; p = 0.023), accompanied by reduced C_m (vitrified GC 58.18 ± 3.17 pF; control GC 77.95 ± 2.88 pF; p = 0.0002) (**fig. S7A-B**). Lending further support to our finding of retained synaptic functionality in field potential recordings from cryopreserved slices (**Fig. 2**), spontaneous synaptic events were recorded regularly from both vitrified PCs and GCs. Moreover, the events occurred at the same frequency that was measured in their control counterparts (**Fig. 3B)**.

To probe firing properties, cells were held at -70 mV by DC injection before ramp-like or rectangular depolarizing current pulses were delivered. Ramp depolarization (0 to 100 pA within 2 s) revealed a marked increase in the current threshold evoking the first AP (i.e. rheobase) in vitrified PCs, whereas no such change was seen in vitrified GCs (**Fig. 3C**). Elevated rheobase in CA1 PCs was accompanied by reduced AP firing during ramps (**Fig. 3C**). When tested with rectangular depolarizing steps 1 s long, decreased firing in vitrified PCs became evident at smaller depolarizations (50 and 100 pA), but disappeared with larger steps (150 and 200 pA, **Fig. 3D**). Closer examination of AP waveforms from vitrified PCs revealed enhanced discharge threshold and increased afterhyperpolarization (AHP) as two potential mechanisms rendering these neurons less excitable than their untreated counterparts (**fig. S7E-I**). As vitrification did not impair hippocampal GC discharge pattern, we were surprised to find their AP waveforms differed from untreated controls in several respects including decreased threshold, faster rise time and smaller half-width (**fig. S7E-I**). Together with the reduced membrane capacitance, which makes the cell electrically more compact, these changes might result from reduced metabolic capacity, or reflect an adaptive process to reinstitute regular GC firing after vitrification (**Fig. 3C-D**).

The absence of neurophysiological signs of hyperexcitability, let alone seizure-like phenomena, in our field potential and whole-cell recordings from two distinct hippocampal regions strongly argues for an intact inhibitory network after vitrification. To substantiate this notion, we made whole-cell recordings from interneurons in the CA1 pyramidal cell layer of cryopreserved slices (n = 12 interneurons; **fig. S8**). These interneurons were characterized by low capacitance (26.67 ± 1.92 pF) and high input resistance (767.08 ± 156.86 MΩ). At rest, they were either quiet with an RMP of -67.56 ± 1.97 mV (n = 5; **fig. S8A**), or fired action potentials tonically (n = 5) or in bursts (n = 2) (**fig. S8C-D**). When held at -70 mV, the silent interneurons discharged 31.11 ± 8.86 APs (n = 5) in response to a 50 pA depolarizing current injection (for 1 s) (**fig. S8B**). Together with our above findings, we take the fact that this sample from just one small hippocampal subregion brought to light different types of apparently healthy interneurons as tentative evidence that vitrification does not harm inhibition.

Discussion

Our results demonstrate the functional recovery of adult mouse hippocampal brain tissue after cryopreservation by vitrification with retained morphological integrity, mitochondrial respiration

255 and electrophysiological activity, including synaptic transmission and plasticity. Normal spontaneous synaptic events revealed that brain activity re-initializes after cessation of all continuous dynamical processes in the vitreous state. Our work improves substantially upon previous attempts at cryopreserving adult brain tissue (*27, 28, 32*), in that vitrification was well tolerated, enabling full or near-physiological recovery of the various indices of intact synaptic
260 transmission and cellular excitability. Previous electrophysiological recordings in neural tissue have focused on freezing (*27, 28, 30*), accompanied by a loss of synaptic connections (*31*). Using vitrification, not only was neural excitability recovered, but also synaptic transmission with the induction of robust LTP. Of note, the slices did tolerate a minimal degree of cooling phase crystallization (**Movie S9**). While vitrification has been applied successfully to peripheral organs
265 (*11-13*), our study encourages its application in the central nervous system.

Notwithstanding the exceptional reinstitution of normal hippocampal functionality in the cryopreserved slices, we noted some differences in principal neurons from the CA1 region and the dentate gyrus weathered vitrification. While pyramidal cells from CA1 exhibited reduced excitability as indicated by increased rheobase and reduced AP firing, GCs from the dentate
270 gyrus maintained normal discharge properties post-vitrification. The different sensitivity to the vitrification process might be due to variations in cell size, membrane properties, or intrinsic metabolic activity, as such variations could in turn result in different osmotic behaviour during CPA loading and unloading as well as in different susceptibility to direct CPA toxicity and chilling injury, e.g., by cold denaturation (*44*).

275 The peak concentration of V3 induced a dose-dependent reduction of the basal respiration and maximal respiratory capacity, indicating peak cryoprotectant toxicity as a cause of mitochondrial stress. Transient mitochondrial stress after vitrification was also implied by ultrastructural swelling of this organelle in electron microscopy. Of note, comparative biology suggests mitochondria play an important role in the adaptation to cold, e.g., in the canadian wood frog
280 (*47*), or in insects (*48*). NMDA receptors have been shown to be sensitive to chilling (*49*), yet both SC-CA1 synapses and mPP-DG synapses, which express NMDA receptor-dependent LTP, showed reliable synaptic potentiation post-vitrification. Understanding these differences between cell types and between vitrified and untreated controls seems difficult, as hypothermia alone affects nearly every investigated biological pathway (*50*). It is likely the case that hypothermia
285 during slicing combined with a brief rewarming and 30 min recovery phase at RT confers some protective preconditioning due to a cold-shock response (*50*).

A limitation of our study is the short observation period of acute brain slices post-vitrification due to their natural deterioration after 10 hours. Further research is needed to extend this period, e.g., using organotypic slice cultures and to characterize the transcriptional and translational
290 effects of vitrification.

In conclusion, we demonstrate that the brain is remarkably robust not only to near-complete shutdown by hypothermia, but even to a complete shutdown in the vitreous state at -196 °C. This reinforces the tenet of brain function being an emergent property of brain structure, and hints at the potential for clinical applications (*14, 15*).

295

References and Notes

1. J. R. Planché, R. Doyle, E. Dalziel, G. Dalziel, C. Perrault, *An Old Fairy Tale: The Sleeping Beauty*. (George Routledge and Sons, London; New York, 1868).

2. E. About, *L'homme à l'oreille cassée*. (L. Hachette et cie., Paris, 1862).
3. A. Percy, S. Widman, J. A. Rizzo, M. Tranquilli, J. A. Elefteriades, Deep hypothermic circulatory arrest in patients with high cognitive needs: full preservation of cognitive abilities. *Ann Thorac Surg* **87**, 117-123 (2009).
4. W. Behringer *et al.*, Survival without brain damage after clinical death of 60-120 mins in dogs using suspended animation by profound hypothermia. *Crit Care Med* **31**, 1523-1531 (2003).
5. W. Denk, K. L. Briggman, M. Helmstaedter, Structural neurobiology: missing link to a mechanistic understanding of neural computation. *Nature Reviews Neuroscience* **13**, 351-358 (2012).
6. W. Russell, R. Burch, *The Principles of Humane Experimental Technique*. (UFAW Publications, Hertfordshire, 1959).
7. M. H. Laporte, N. Klena, V. Hamel, P. Guichard, Visualizing the native cellular organization by coupling cryofixation with expansion microscopy (Cryo-ExM). *Nature Methods* **19**, 216-222 (2022).
8. N. Korogod, C. C. H. Petersen, G. W. Knott, Ultrastructural analysis of adult mouse neocortex comparing aldehyde perfusion with cryo fixation. *eLife* **4**, e05793 (2015).
9. G. M. Fahy *et al.*, Physical and biological aspects of renal vitrification. *Organogenesis* **5**, 167-175 (2009).
10. A. Chiu-Lam, E. Staples, C. J. Pepine, C. Rinaldi, Perfusion, cryopreservation, and nanowarming of whole hearts using colloidally stable magnetic cryopreservation agent solutions. *Sci Adv* **7**, (2021).
11. A. Sharma *et al.*, Cryopreservation of Whole Rat Livers by Vitrification and Nanowarming. *Ann Biomed Eng* **51**, 566-577 (2023).
12. Z. Han *et al.*, Vitrification and nanowarming enable long-term organ cryopreservation and life-sustaining kidney transplantation in a rat model. *Nat Commun* **14**, 3407 (2023).
13. B. Wowk, J. Phan, R. Pagotan, E. Galvez, G. M. Fahy, 27 MHz constant field dielectric warming of kidneys cryopreserved by vitrification. *Cryobiology* **115**, 104893 (2024).
14. S. Bojic *et al.*, Winter is coming: the future of cryopreservation. *BMC Biology* **19**, 56 (2021).
15. O. M. Moen, The case for cryonics. *J Med Ethics* **41**, 677-681 (2015).
16. T. Nagel, What is it like to be a bat? *Philosophical Review* **83**, 435-450 (1974).
17. D. Chalmers, Facing up to the problem of consciousness. *Journal of Consciousness Studies* **2**, 200-219 (1995).
18. J. Kleiner, E. Hoel, Falsification and consciousness. *Neuroscience of Consciousness* **2021**, (2021).
19. B. Luyet, F. Gonzales, Growth of nerve tissue after freezing in liquid nitrogen. *Biodynamica* **7**, 171-174 (1953).
20. R. J. Robbins *et al.*, Cryopreservation of human brain tissue. *Experimental Neurology* **107**, 208-213 (1990).
21. S. Jensen, T. Sørensen, J. Zimmer, Cryopreservation of fetal rat brain tissue later used for intracerebral transplantation. *Cryobiology* **24**, 120-134 (1987).
22. F. Otto, P. Görtz, W. Fleischer, M. Siebler, Cryopreserved rat cortical cells develop functional neuronal networks on microelectrode arrays. *Journal of Neuroscience Methods* **128**, 173-181 (2003).
23. S. Heumüller-Klug *et al.*, Impact of cryopreservation on viability, gene expression and function of enteric nervous system derived neurospheres. *Front Cell Dev Biol* **11**, 1196472 (2023).

24. W. Ma, T. O'Shaughnessy, E. Chang, Cryopreservation of adherent neuronal networks. *Neuroscience Letters* **403**, 84-89 (2006).
25. M. Uemura, H. Ishiguro, Freezing behavior of adherent neuron-like cells and morphological change and viability of post-thaw cells. *Cryobiology* **70**, 122-135 (2015).
26. J.-F. Brunet, L. Pellerin, P. Magistretti, J.-G. Villemure, Cryopreservation of human brain tissue allowing timely production of viable adult human brain cells for autologous transplantation. *Cryobiology* **47**, 179-183 (2003).
27. I. Suda, K. Kito, C. Adachi, Viability of long term frozen cat brain in vitro. *Nature* **212**, 268-270 (1966).
28. I. Suda, K. Kito, C. Adachi, Bioelectric discharges of isolated cat brain after revival from years of frozen storage. *Brain Research* **70**, 527-531 (1974).
29. J. E. Pascoe, A. S. Parkes, The survival of the rat's superior cervical ganglion after cooling to –76° C. *Proceedings of the Royal Society of London. Series B - Biological Sciences* **147**, 510-519 (1957).
30. W. Xue *et al.*, Effective cryopreservation of human brain tissue and neural organoids. *Cell Reports Methods* **4**, (2024).
31. N. A. Ivlicheva, I. A. Chistopolskiy, L. I. Kramarova, E. N. Gakhova, Electrophysiological activity of the brain of the mollusk Lymnaea stagnalis L. after cryopreservation in liquid nitrogen (−196°C). *Biochemistry (Moscow) Supplement Series A: Membrane and Cell Biology* **8**, 324-333 (2014).
32. Y. Pichugin, G. M. Fahy, R. Morin, Cryopreservation of rat hippocampal slices by vitrification. *Cryobiology* **52**, 228-240 (2006).
33. G. M. Fahy, D. R. MacFarlane, C. A. Angell, H. T. Meryman, Vitrification as an approach to cryopreservation. *Cryobiology* **21**, 407-426 (1984).
34. B. Wowk, Thermodynamic aspects of vitrification. *Cryobiology* **60**, 11-22 (2010).
35. G. M. Fahy, in *Fertility Preservation: Principles and Practice,* J. Donnez, S. S. Kim, Eds. (Cambridge University Press, Cambridge, 2021), pp. 49-66.
36. J. Farrant, Mechanism of Cell Damage During Freezing and Thawing and its Prevention. *Nature* **205**, 1284-1287 (1965).
37. B. J. Luyet, M. P. Gehenio, *Life and Death at Low Temperatures*. (Biodynamica, 1940).
38. W. F. Rall, G. M. Fahy, Ice-free cryopreservation of mouse embryos at -196 degrees C by vitrification. *Nature* **313**, 573-575 (1985).
39. G. M. Fahy *et al.*, Cryopreservation of organs by vitrification: perspectives and recent advances. *Cryobiology* **48**, 157-178 (2004).
40. H. Woelders, Effect of the flow-force relationships used in two parameter modelling of freezing and vitrification protocols for bovine embryos. *Cryobiology* **117**, 104973 (2024).
41. H. Y. Elmoazzen, J. A. Elliott, L. E. McGann, Osmotic transport across cell membranes in nondilute solutions: a new nondilute solute transport equation. *Biophys J* **96**, 2559-2571 (2009).
42. J. D. Benson, A. J. Kearsley, A. Z. Higgins, Mathematical optimization of procedures for cryoprotectant equilibration using a toxicity cost function. *Cryobiology* **64**, 144-151 (2012).
43. G. M. Fahy, J. Saur, R. J. Williams, Physical problems with the vitrification of large biological systems. *Cryobiology* **27**, 492-510 (1990).
44. P. L. Privalov, Cold denaturation of proteins. *Crit Rev Biochem Mol Biol* **25**, 281-305 (1990).
45. Z. Han *et al.*, Kidney tissue loading reduces the critical cooling and warming rates of VS55 and VMP cryoprotective solutions. *Cryobiology* **117**, 104977 (2024).

46. W. F. Rall, D. S. Reid, J. Farrant, Innocuous biological freezing during warming. *Nature* **286**, 511-514 (1980).
47. J. M. Storey, S. Wu, K. B. Storey, Mitochondria and the Frozen Frog. *Antioxidants (Basel)* **10**, (2021).
48. J. Lubawy, S. Chowański, Z. Adamski, M. Słocińska, Mitochondria as a target and central hub of energy division during cold stress in insects. *Front Zool* **19**, 1 (2022).
49. A. A. Mokrushin, Effect of Cryopreservation Time on the Activity of Ionotropic Glutamatergic Mechanisms: An in vitro Study. *Biology Bulletin* **47**, 71-79 (2020).
50. M. A. Yenari, H. S. Han, Neuroprotective mechanisms of hypothermia in brain ischaemia. *Nat Rev Neurosci* **13**, 267-278 (2012).
51. F. Zheng *et al.*, Activin tunes GABAergic neurotransmission and modulates anxiety-like behavior. *Mol Psychiatry* **14**, 332-346 (2009).
52. Y. Pichugin, www.cryonics.org/research/blood-brain-barrier-preliminary-patent-application-disclosure. (2007).
53. A. German, E. Y. Akdaş, Excitability and synaptic transmission after vitrification of mouse corticohippocampal slices. *bioRxiv*, 2024.2006.2003.597218 (2024).
54. P. Virtanen *et al.*, SciPy 1.0: fundamental algorithms for scientific computing in Python. *Nature Methods* **17**, 261-272 (2020).

Acknowledgments: We thank Andrea Eichhorn, Elke Kretzschmar, Maria Schulte and Birgit Vogler for technical help.

Funding:

German Society of Cryobanks (AG, JW)

German Research Foundation grants SFB 1483, FOR 5534 (AG)

Interdisciplinary Center for Clinical Research Erlangen project J111 (AG), ELAN project P166-26514166 (EYA)

Author contributions: AG optimized and performed the vitrification procedures. EYA performed metabolic analysis and preliminary electrophysiological experiments; CFK conducted electron microscopy; FZ designed and performed electrophysiological experiments and data analysis; AG initiated the project with the help of EYA and AF; AF, JW, and CA supervised the project; AG, CA and FZ wrote the manuscript.

Competing interests: Authors declare that they have no competing interests.

Data and materials availability: Data of this study is available from the corresponding author upon reasonable request.

Supplementary Materials

Materials and Methods

Supplementary Text

Figs. S1 to S8

Tables S1 to S3

Movies S1 to S12
Suppl_Movies

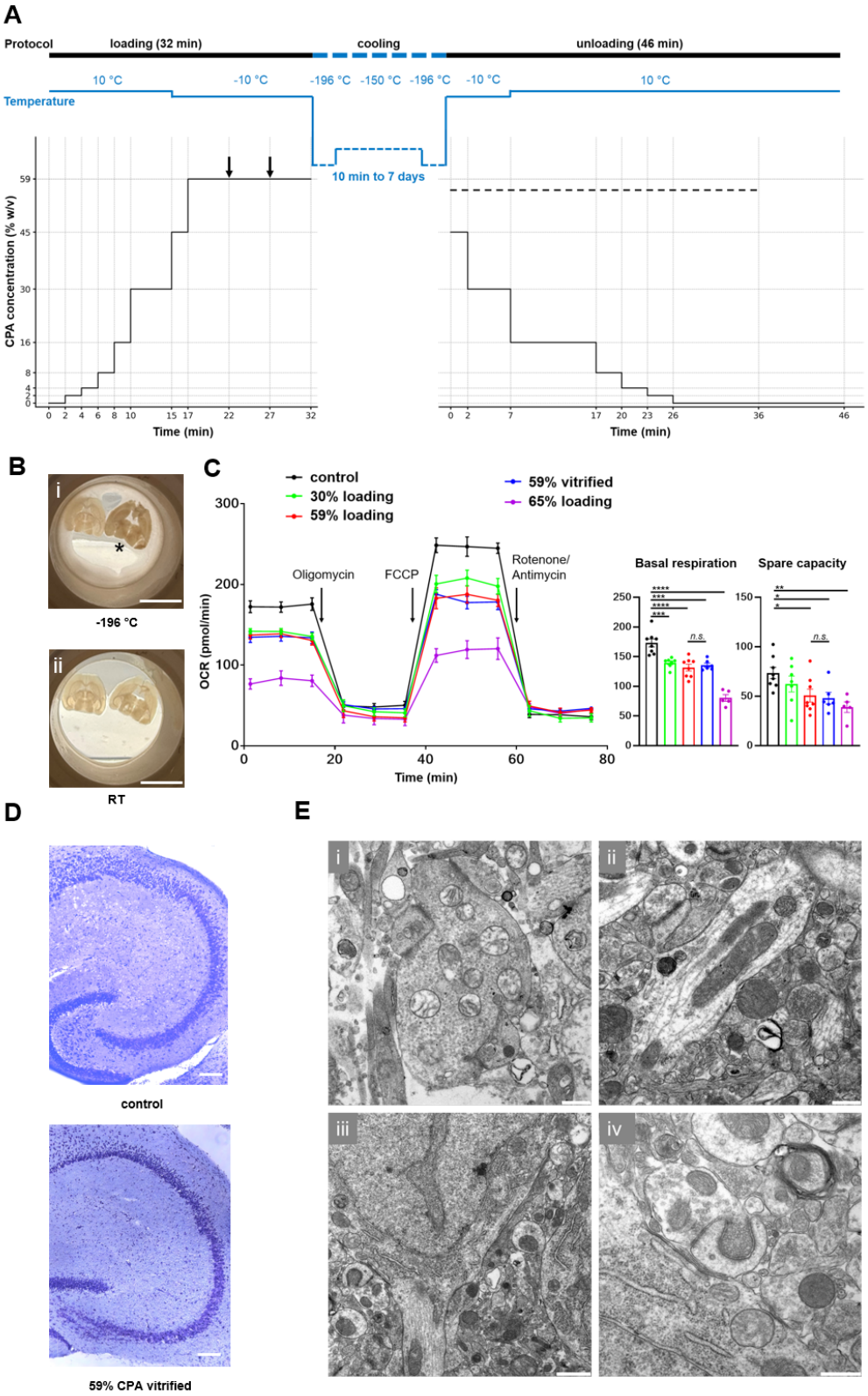
A
Protocol
loading (32 min)
cooling
unloading (46 min)
10 °C
-10 °C
-196 °C
-150 °C
-196 °C
-10 °C
10 °C
Temperature
10 min to 7 days
CPA concentration (% w/v)
Time (min)
Time (min)
B
i
-196 °C
ii
RT
C
control
30% loading
59% loading
59% vitrified
65% loading
Oligomycin
FCCP
Rotenone/
Antimycin
OCR (pmol/min)
Time (min)
Basal respiration
Spare capacity
n.s.
n.s.
D
control
59% CPA vitrified
E
i
ii
iii
iv

440 **Fig. 1. Vitrification of adult mouse brain slices.** (**A**) Time course of vitrification protocol, with varied temperature (**top**) and CPA concentration (**bottom**). Arrows indicate where transfer to fresh vitrification solution occurs. Dotted line indicates addition of 300 mM mannitol to the carrier solution for unloading. (**B**) Brain slices (350 µm thick) inside mesh at liquid nitrogen temperature (**i**; at -196 ºC*)* demonstrating apparent vitrification (glossy and transparent) vs. crystallization (dull and opaque; asterisk). Such difference in appearance disappeared after the
445 rewarming process (**ii**; 5 min exposure to RT). (**C**) Concentration-dependent effect of CPA loading on oxygen consumption rates (OCR) of mouse hippocampal tissue. 0-20 min: Basal respiration. 20-40 min: Ablation of ATP-linked respiration with Oligomycin. 40-60 min: Maximal respiratory capacity induced with FCCP, 60-80 min: Non-mitochondrial respiration induced with rotenone and antimycin A. Note that the vitrification with 59% w/v V3 did not affect metabolism compared to incubation with 59% w/v V3 alone. Statistical comparisons were performed with
450 one-way ANOVA followed by Dunnet's test, *<0.05 **p<0.005 ***p<0.0005 ****p<0.0001. (**D**) Nissl staining of hippocampal sections (30 µm) without treatment (control; **top**) and after vitrification (5 hours post-rewarming; **bottom**) indicated the cytoarchitectural integrity. **(E**) Electron microscopy revealed well-preserved ultrastructure in the CA1 region of the vitrified hippocampus. Immediately after completion of the vitrification protocol and CPA unloading, occasional astroglial and mitochondrial swelling was observed (**i**). After 10 hours of incubation in aCSF
455 at RT, the ultrastructure, including mitochondria and synapses (**ii**), dendrite and neuron (**iii**), synapse and myelin (**iv**) is indistinguishable from control slices. Scale bars: 1 cm (**B**); 100 µm (**D**); 0.5 µm (**i, ii, iv; E**), 1 µm (**iii; E**).

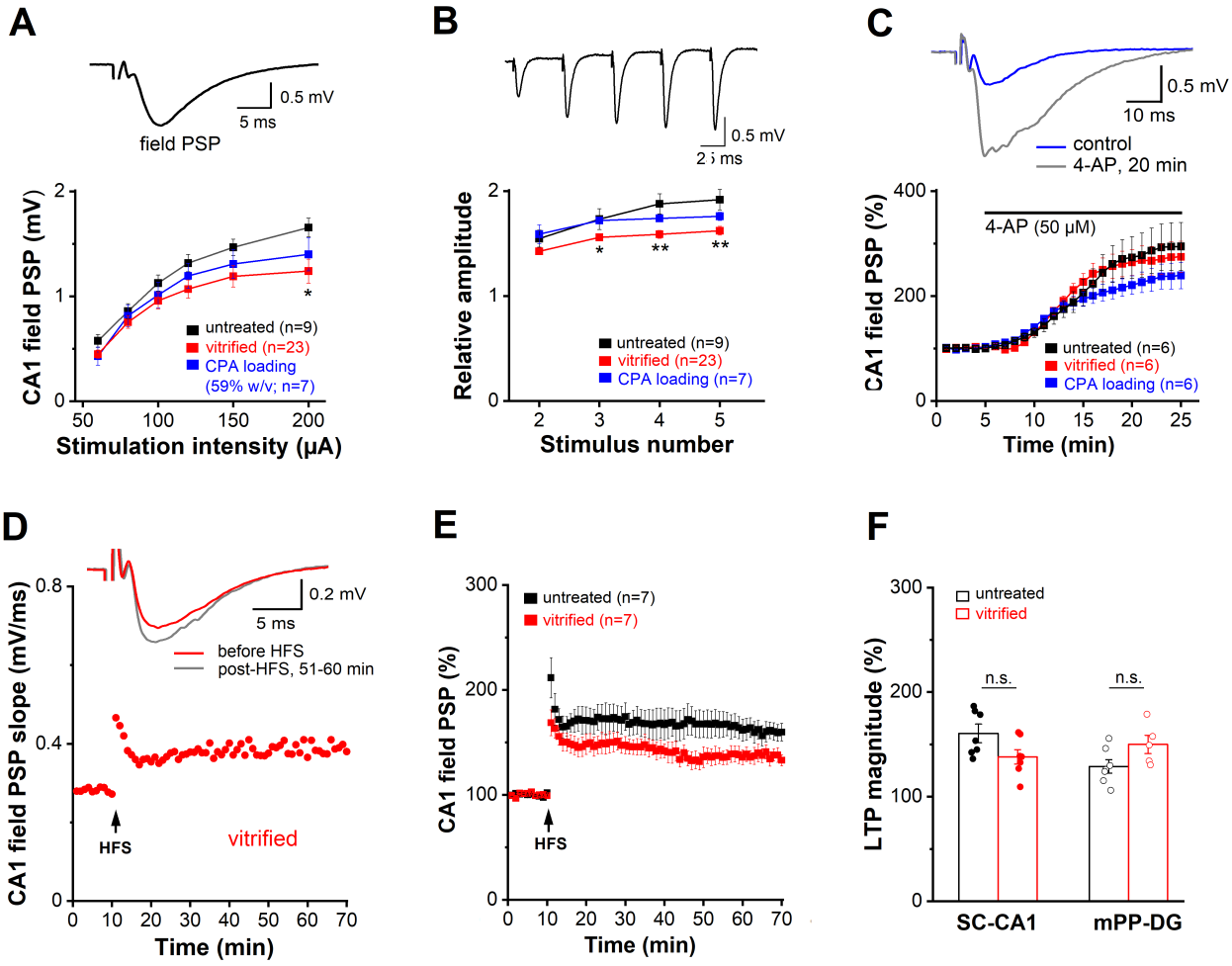

Fig. 2. Recovery of synaptic functions after vitrification and rewarming. Field postsynaptic potentials (field PSP or fPSP) were evoked by electrical stimulation of Schaffer collaterals (SC) and monitored in CA1 stratum radiatum. **(A)** Input-output (I-O) curves from untreated slices, CPA loading controls, and vitrified slices. The inset on top illustrates typical field PSP response in an untreated slice (stimulus strength 75 µA). (**B**) Effects of vitrification and CPA loading alone on short-term synaptic plasticity (STP). Same groups as in (**A**). Inset on top illustrates characteristic facilitation of fPSPs during STP-inducing stimulation (untreated slice, 70 µA). (**C**) Time course of fPSP augmentation during bath application of 4-AP (50 µM) in untreated slices, loading controls, and vitrified slices. Inset on top depicts effect of 4-AP on fPSP in slice with CPA loading alone. (**D-E**) LTP of SC-CA1 synapses in untreated controls and vitrified slices. Inset in (**D**) illustrates averaged voltage traces before and 51-60 min post high frequency stimulation (HFS). **(F)** Histogram depicts LTP magnitude as percentage increase in field PSP slope relative to baseline before HFS at the SC-CA1 and the mPP-GC synapse. Statistical comparisons were performed with one-way ANOVA followed by Tukey's post-hoc test or Student t-test. N.s. not significant; * $p < 0.05$; ** $p < 0.01$.

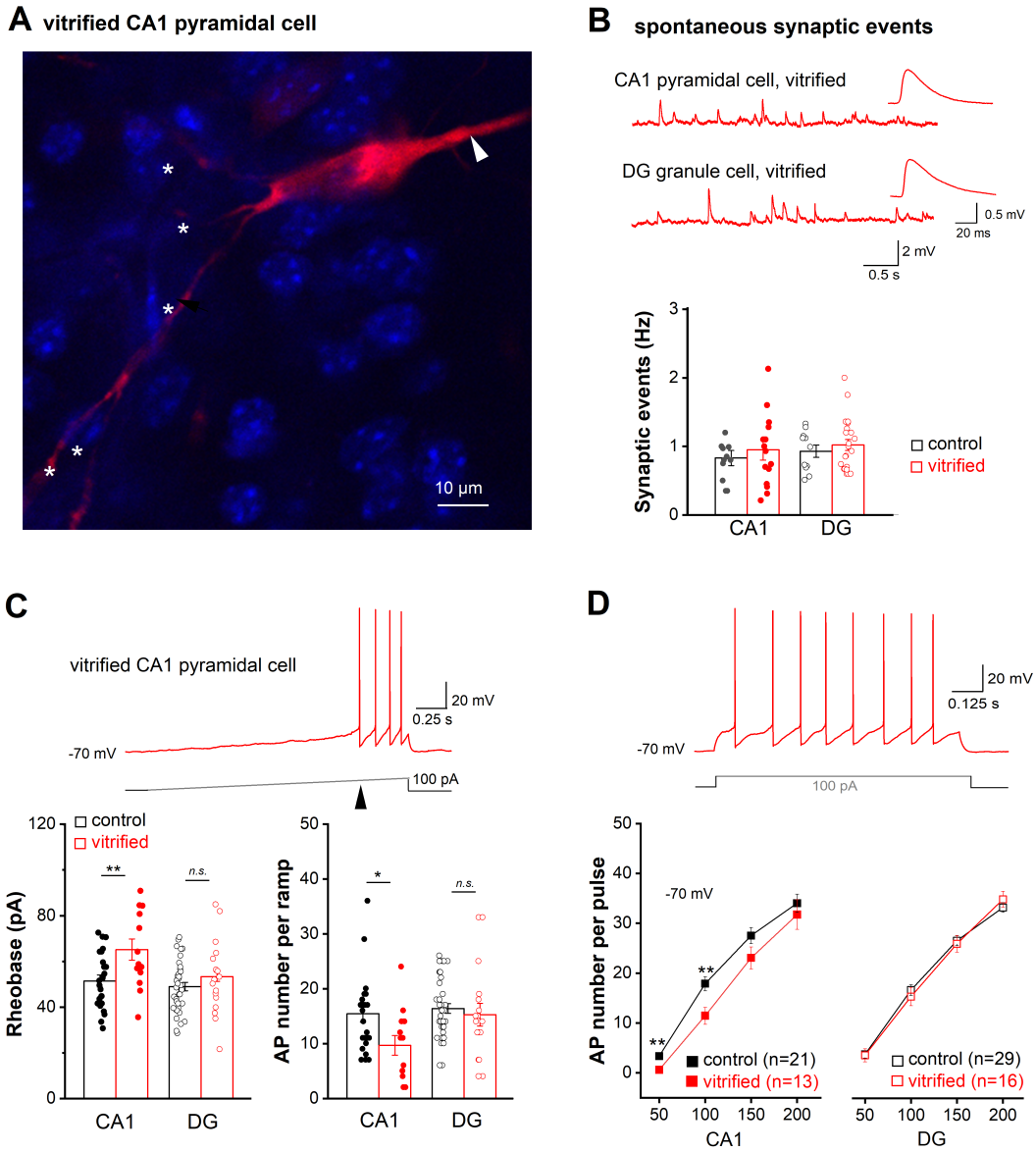
A vitrified CA1 pyramidal cell
10 µm
B spontaneous synaptic events
CA1 pyramidal cell, vitrified
DG granule cell, vitrified
0.5 mV
20 ms
2 mV
0.5 s
Synaptic events (Hz)
control
vitrified
CA1
DG
C
vitrified CA1 pyramidal cell
20 mV
0.25 s
-70 mV
100 pA
Rheobase (pA)
AP number per ramp
**
n.s.
*
D
20 mV
0.125 s
-70 mV
100 pA
AP number per pulse
control (n=21)
vitrified (n=13)
control (n=29)
vitrified (n=16)

Fig. 3. Recovery of cellular excitability and spontaneous synaptic activity after vitrification and rewarming. Whole-cell current-clamp recordings were performed from CA1 pyramidal cells and dentate gyrus (DG) granule cells. **(A)** Biocytin-filled CA1 pyramidal cell from a vitrified slice was stained with Cy3-coupled streptavidin (red). Arrowhead and asterisks point to apical dendrite and basal dendrites, respectively. Nuclei were stained with DAPI (blue). **(B)** Frequency of spontaneous synaptic events in CA1 and DG cells did not differ between control and vitrified slices. The traces above the histogram exemplify events in individual recordings taken at resting membrane potential. Insets depict averaged waveforms of spontaneous synaptic events at higher magnification. (**C-D**) Action potential (AP) firing was elicited using depolarizing currents delivered as ramps (C) or rectangular steps (D) from membrane potential adjusted to -70 mV. Arrowhead in current trace of (C) indicates rheobase. Histograms show that vitrification altered firing properties only in CA1 pyramidal cells, but not in DG granule cells. Statistical comparisons were performed using unpaired, two-tailed student's t-test (**B, C**) or one-way ANOVA followed by Tukey's post-hoc test (**D**). n.s. not significant; * $p < 0.05$; ** $p < 0.01$.

Supplementary Materials for

Functional recovery of adult brain tissue arrested in time during cryopreservation by vitrification

Alexander German, Enes Yağız Akdaş, Cassandra Flügel-Koch, Anna Fejtova, Jürgen Winkler, Christian Alzheimer, Fang Zheng

Corresponding author: alex.german@fau.de

The PDF file includes:

Materials and Methods
Supplementary Text
Figs. S1 to S8
Tables S1 to S3

Other Supplementary Materials for this manuscript include the following:

Movies S1 to S12
Suppl_Movies

Materials and Methods

Animals

Adult male C57BL/6J mice (3-6-month-old) were used in this study. Mice were maintained under standard laboratory conditions, which included a 12/12 light/dark cycle with lights on at 06:00, a temperature of 22 ± 1 °C, and 60% humidity, with water and food available ad libitum. All experiments were conducted in accordance with the guidelines for the Care and Use of Laboratory Animals set by the Local Government of Unterfranken and the European Communities Council Directive (2010/63/EU).

Brain slice preparation and vitrification

Horizontal slices containing the hippocampus were prepared from mice anesthetized with isoflurane, as described previously (*51*). Briefly, 350 µm thick brain slices were cut using a Leica VT1200 Vibratome (Leica Biosystems, Germany) in ice-cold sucrose-based artificial cerebrospinal fluid (aCSF) containing (in mM) 75 sucrose, 87 NaCl, 3 KCl, 0.5 $CaCl_2$, 7 $MgCl_2$, 1.25 NaH_2PO_4, 25 $NaHCO_3$ and 10 D-glucose. Slices were incubated in the same solution for 10 min at 35 ºC and then maintained in aCSF containing (in mM) 125 NaCl, 3 KCl, 1 $CaCl_2$, 3 $MgCl_2$, 1.25 NaH_2PO_4, 25 $NaHCO_3$ and 10 D-glucose at room temperature (RT). All solutions were constantly gassed with 95% O_2 - 5% CO_2 to keep pH constant (7.4).

After a 30-minute recovery phase, the slices were transferred into a Netwell polyester mesh insert (Corning, USA) for 6-well plates with mesh size 74 µm. The 6-well plate was positioned on the surface of a water bath inside a polystyrene box (set to 10 °C by mixing tap water and ice). Brain slices within the mesh insert were immersed into 10 °C solutions of increasing concentration of cryoprotectant in a carrier solution. During protocol optimization, we successfully used the CI-VM-1 carrier solution (*52*) and LM5 carrier solution (*32, 39*). All results reported herein were generated with LM5, containing glucose (90 mM), mannitol (45 mM), lactose (45 mM), KCl (8.2 mM), K_2HPO_4 (7.2 mM), reduced glutathione (5 mM), adenine (1 mM), $NaHCO_3$ (10 mM) (**table S1***)*.

Subsequently, the mesh insert carrying the slices was transferred into higher concentrations of the vitrification solution, which was set to -10 °C in a second polystyrene box containing a 65% w/v ethylene glycol in water bath (kept at -10 °C using dry ice). During protocol optimization, we successfully used a 61% w/v ethylene glycol vitrification solution (*53*), a 37.5% w/v ethylene glycol and 12.5% dimethyl sulfoxide vitrification solution (*52*), and a reduced version of the VM3 vitrification solution (*39*), which we call V3. Addition of dimethyl sulfoxide shortened incubation times necessary for vitrification. As V3 resulted in the best functional recovery, the two other CPA compositions were not explored further. All results reported herein were generated with V3 (**table S2**). The w/v concentrations of V3 corresponded to 2.85 M dimethyl sulfoxide, 2.71 M ethylene glycol, 2.86 M formamide, or 8.42 M permeable CPA in total plus 23-35 mM impermeable CPA. 59 g of this solution had a volume of approximately 53.3 ml at 20 °C, and repeated filling and mixing to a total volume of 100 ml required the addition of approximately 49.4 ml of LM5. To assess vitrification stability and toxicity of V3 further, slices were also incubated with final concentrations of 30% w/v = 4.28 M, 45% w/v = 6.42 M, 52% w/v = 7.42 M, 53% w/v = 7.57 M, 54% w/v = 7.71 M, 55% w/v = 7.85 M, 56% w/v = 8.00 M,

565 57% w/v = 8.14 M, 58% w/v =8.28 M and 65% w/v = 9.28 M total V3 CPA and permeable V3 CPA, respectively.

Fig. 1A illustrates the final vitrification protocol: For CPA loading, brain slices were immersed into 10 ml of 10 °C and -10 °C solutions of increasing concentration of cryoprotectant in the
570 LM5 carrier solution: 0% w/v V3 for 2 min, 2% for 2 min, 4% for 2 min, 8% for 2 min, 16% for 2 min and 30% w/v V3 for 5 min each at 10 °C, followed by 45% w/v V3 for 2 minutes and three iterations of 59% w/v V3 for 5 minutes each at -10 °C.

After vitrification on a copper cylinder (**fig. S1**), the mesh insert was slowly transferred into
575 liquid nitrogen at -196 °C, and subsequently transferred into a -150 °C freezer for long-term storage (up to 7 days). For rewarming, slices were slowly transferred into liquid nitrogen again, and subsequently transferred on top of the copper cylinder again. After 5 minutes, the mesh insert was rapidly rewarmed in 100 ml of 52% w/v V3 at -10 °C.

580 For CPA unloading, brain slices were immersed into -10 °C and 10 °C solutions of decreasing concentration of V3 in the carrier solution with additional 300 mM mannitol, followed by a final step of carrier solution without added mannitol:
45% w/v V3 for 2 min and 30% at -10 °C for 5 min, followed by 16% w/v V3 for 10 min, 8% for 3 min, 4% for 3 min, 2% for 3 min, 0% for 10 min at 10 °C each, followed by a final step of
585 LM5 without added mannitol at 10 °C for 10 min (**table S3**)

Metabolic analysis

After cryopreservation using the vitrification protocol, the slices were incubated for 2 hours in carbogenated aCSF at RT to allow recovery. Agilent Seahorse XFe96 analyzer was used to
590 assess oxygen consumption rate (OCR) to elucidate the mitochondrial capacity of the brain slices, using the Seahorse mito-stress test kit according to the manufacturer's instructions. Biopsies were then taken from the CA1 region of the hippocampal slices using 0.75 mm biopsy punches. These biopsy punches were immediately placed into individual wells of a Seahorse islet capture plate, a 96-well plate format filled with aCSF, for OCR measurements. The hippocampi
595 were incubated at 37 °C without CO_2 for 45 min prior to recordings. Baseline OCR recordings were conducted to assess mitochondrial capacity. Following this, the biopsies were sequentially treated with 25 µM of the ATPase pump inhibitor oligomycin to inhibit mitochondrial oxygen consumption, then with 7.5 µM of the ionophore Carbonyl cyanide-p-trifluoromethoxyphenylhydrazone (FCCP) to determine maximal mitochondrial capacity and
600 proton leakage. Finally, a mixture of 5 µM rotenone and 5 µM antimycin A, inhibitors of electron transport chain complexes I and III, respectively, was added to block mitochondrial electron transport.

Light and electron microscopic analysis

605 For visual inspection of slices, a Leica Ivesta 3 videostereomicroscope was used. For light microscopy to evaluate brain structure and neural morphology, the brain slices with standard CPA loading of 59% w/v, with and without vitrification, were fixated with 4% paraformaldehyde overnight at 4 °C, washed, and kept in phosphate buffered saline (PBS). Frozen sections of 30 µm were obtained and stained with cresyl violet (Nissl staining). For electron microscopy, the
610 vitrified slices were fixated in 2% glutaraldehyde and 1% formaldehyde in cacodylate buffer for 24 hours, washed overnight in cacodylate buffer, postfixed with OsO4, dehydrated, and embedded in Epon (Roth, Germany). Semithin sections (1 µm) were stained with toluidine blue.

Ultrathin sections (50 nm) were stained with uranyl acetate and lead citrate and viewed with a Zeiss EM 900N electron microscope.

615

Electrophysiological recordings in the hippocampus

Whole-cell current-clamp recordings and extracellular field potential recordings were performed in the CA1 region and the dentate gyrus (DG) of the hippocampal formation from untreated and treated slices, having rested 1-10 h in the incubating chamber at RT. Individual slices were
620 transferred to a submerged chamber that was mounted on the stage of an upright microscope, and perfused with normal aCSF with 1.5 mM $MgCl_2$ and 2.5 mM $CaCl_2$ at 31 ºC. Recorded signals were filtered at 6 kHz (for action potentials) or 2 kHz (for field potentials) and sampled at 20 kHz using a Multiclamp 700B amplifier together with Digidata 1550A interface and pClamp10.7 software (Molecular Devices, Sunnyvale, CA, USA).

625

Field postsynaptic potentials (fPSPs) in CA1 stratum radiatum and DG middle molecular layer were recorded with a glass pipette filled with modified aCSF, in which $NaHCO_3$ was replaced by HEPES (5 mM) to avoid pH change. A concentric platinum bipolar electrode was inserted into the stratum radiatum to stimulate Schaffer collaterals (SC), or into DG molecular layer to
630 stimulate medial perforant path (mPP), using constant current pulses 0.1 ms wide. The input-output relationship of fPSPs was routinely determined by stepwise increase in stimulus strength from 50 to 200 µA. Short-term potentiation (STP) was examined using a brief stimulus train consisting of 5 pulses at 20 Hz. During baseline recording, strength of electrical stimuli, which were delivered at 0.1 Hz, were adjusted to elicit 30-40% of the maximum response. Long-term
635 potentiation (LTP) of the SC-CA1 synapse was induced by means of high frequency stimulation (HFS, 100 Hz for 1s, repeated once after 20 s). LTP of the mPP-DG synapse required stronger HFS (100 Hz x 1s, repeated 4 times at 10 s intervals) to overcome robust GABAergic inhibition in this area. fPSPs were monitored for 60 min post HFS, and data points were obtained by averaging six responses every minute. Slopes were calculated from rising phase (20-80%) of
640 fPSPs, normalized as percentage of baseline value, and pooled across experiments of the same group.

Whole-cell current-clamp recordings were performed on visually identified cells in CA1 and DG of dorsal hippocampal slices. Patch pipettes were filled with (in mM) 135 K-gluconate, 5
645 HEPES, 3 $MgCl_2$, 5 EGTA, 2 Na_2ATP, 0.3 Na_3GTP, 4 NaCl (pH 7.3). Electrode resistance with internal solution in bath was 3-5 MΩ. After Giga-seal formation, whole-cell configuration was achieved by membrane rupture in voltage-clamp mode (Vh -70 mV). Hippocampal cell properties, including membrane capacitance and input resistance (Rm), were collected 2-3 min later with a 'membrane test' protocol' delivering 10 mV biphasic pulses. Rm was re-examined
650 after switching to current-clamp mode using hyperpolarizing pulses (5 mV). Spontaneous postsynaptic events were collected at resting membrane potential (RMP). All potentials were corrected for liquid junction potential. To test cell excitability, depolarizing pulses (50, 100, 150 and 200 pA for 1 s) and ramps (from 0 to 100 pA within 2 s) were used to elicit action potentials (AP), with membrane potential initially held at -70 mV by injecting current.

655

Electrophysiological data analysis was performed off-line with Clampfit 10.7 (Molecular Devices, CA, USA). Peak amplitude and slope (20-80% of rising phase) of field PSPs were used to quantify basic features of synaptic transmission (e.g. input-output curve) and LTP magnitude, respectively. For cell excitability, the number of APs during steps or ramps was calculated.
660 Rheobase was determined as minimal current necessary to elicit 1st AP during ramps. AP

parameters were analyzed for the first AP after depolarizing pulse (100 pA). Spontaneous synaptic events were detected using an automated event detection algorithm to quantify frequency, amplitude and kinetics of synaptic inputs.

665 Biocytin labelling

In some experiments, 1% biocytin (BioTrend Chemicals GmbH, Cologne, Germany) was included in whole-cell recording solution. The recording pipette was carefully retracted at the end of the experiment, and the slice was fixed with 4% paraformaldehyde overnight at 4 ºC. The slices were then washed several times with 0.1 M phosphate buffer (PBS) and kept in PBS.
670 Blocking and permeabilization was performed by using a PBS-based blocking buffer, containing 1% bovine serum albumin, 0.5% Triton X-100 and Cy3 coupled streptavidin (Cy™3 Streptavidin, 1:1000, Jackson Immuno Research, Suffolk, UK) overnight. After PBS washing, the slices were mounted with Roti®-Mount FluorCare DAPI on cover slips. Confocal imaging was performed on a Zeiss LSM 780 confocal microscope by using 20x and 63x objectives.
675 Fluorophores were excited at 561 nm wavelength. ZEN 2010 and ImageJ software were used for editing confocal images.

Statistics

Data were expressed as means ± SEM. OriginPro 2021G (OriginLab Corporation, MA, USA)
680 was used for electrophysiological statistics and figures. Shapiro-Wilk test was used to assess normality of data distribution, and the null hypothesis was accepted when p-value was larger than 0.05. Statistical comparisons were performed using unpaired or paired Student's t-test and one-way analysis of variance (ANOVA) followed by Tukey's post-hoc test, as appropriate. Significance was assumed for $p < 0.05$. Spearman rank-order correlation coefficient of OCR
685 measurements was performed using the spearmanr and permutation_test function from the SciPy library (version 1.14.1) in Python (*54*).

Supplementary Text

690 Abbreviations

aCSF, artificial cerebrospinal fluid; AP, action potential; CPA, cryoprotective agent; DG, dentate gyrus; DMSO, dimethyl sulfoxide; EG, ethylene glycol; fAHP, fast afterhyperpolarization; fPSP, field postsynaptic potential; LTP, long-term potentiation; OCR, oxygen consumption rate; RMP, resting membrane potential; Rm, membrane input resistance; RT, room temperature; SC,
695 Schaffer Collaterals; spPSP, spontaneous postsynaptic potential; STP, short-term plasticity

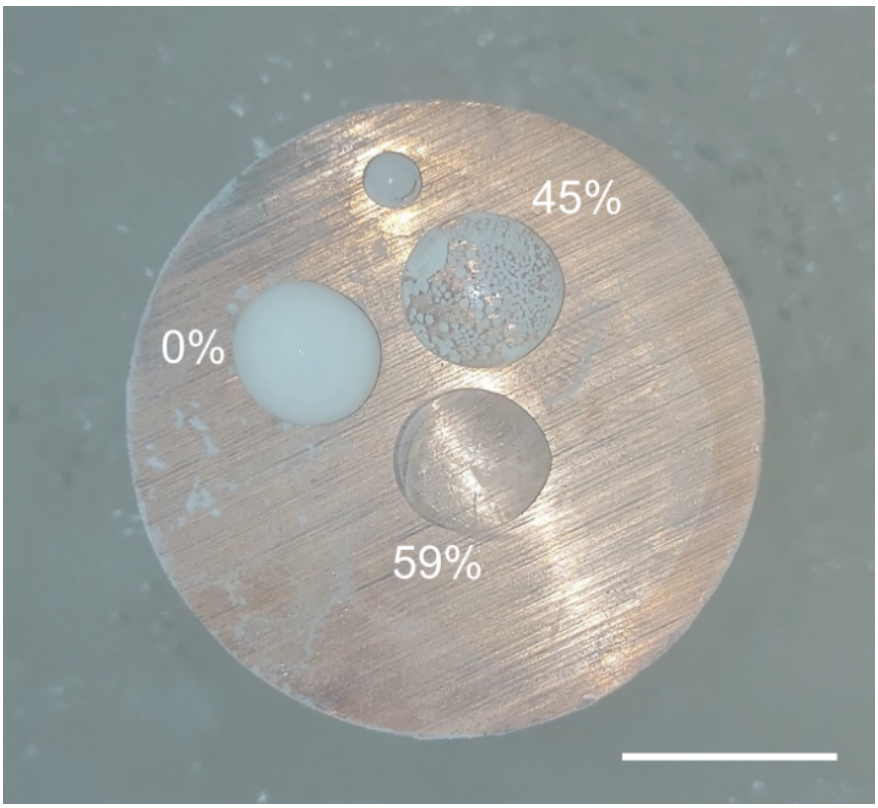

Fig. S1. Vitrification on copper cylinder

For directional cooling, a copper cylinder was immersed in liquid nitrogen (view from above). 1 ml droplets of LM5 carrier solution with 0% w/v V3 shows complete crystallization, 45% w/v partially crystalline, partially vitreous, 59% is completely vitreous. No cracking occurred during directional cooling from below. Scale bar 1 cm.

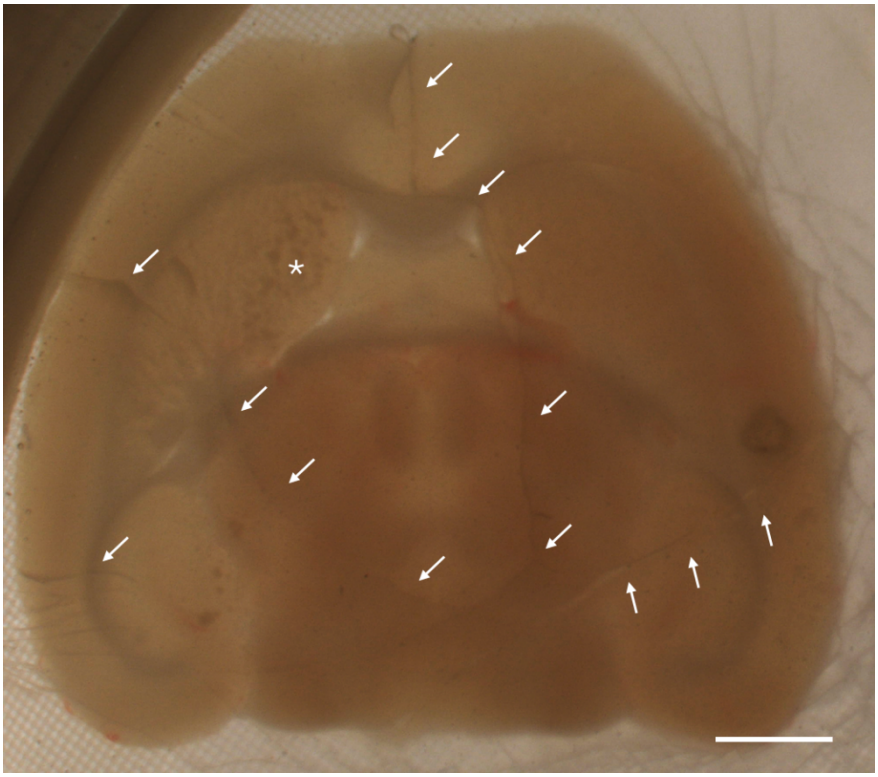

Fig. S2. Damage from cracking due to thermomechanical stress and crystallization

Destruction of brain slices due to cracking during direct immersion in liquid nitrogen. Tissue cracks are visible at cryogenic temperature and marked with white arrows. A limited degree of cooling phase crystallization is visible in the striatum on the left side of the image (asterisk). A limited degree of diffuse rewarming phase crystallization is visible on the right side of the image (diffuse darkening). Stereo microscopy with -160 °C isopentane covering. Lighting from behind. Image contrast enhanced by 42%. Scale bar 1 mm.

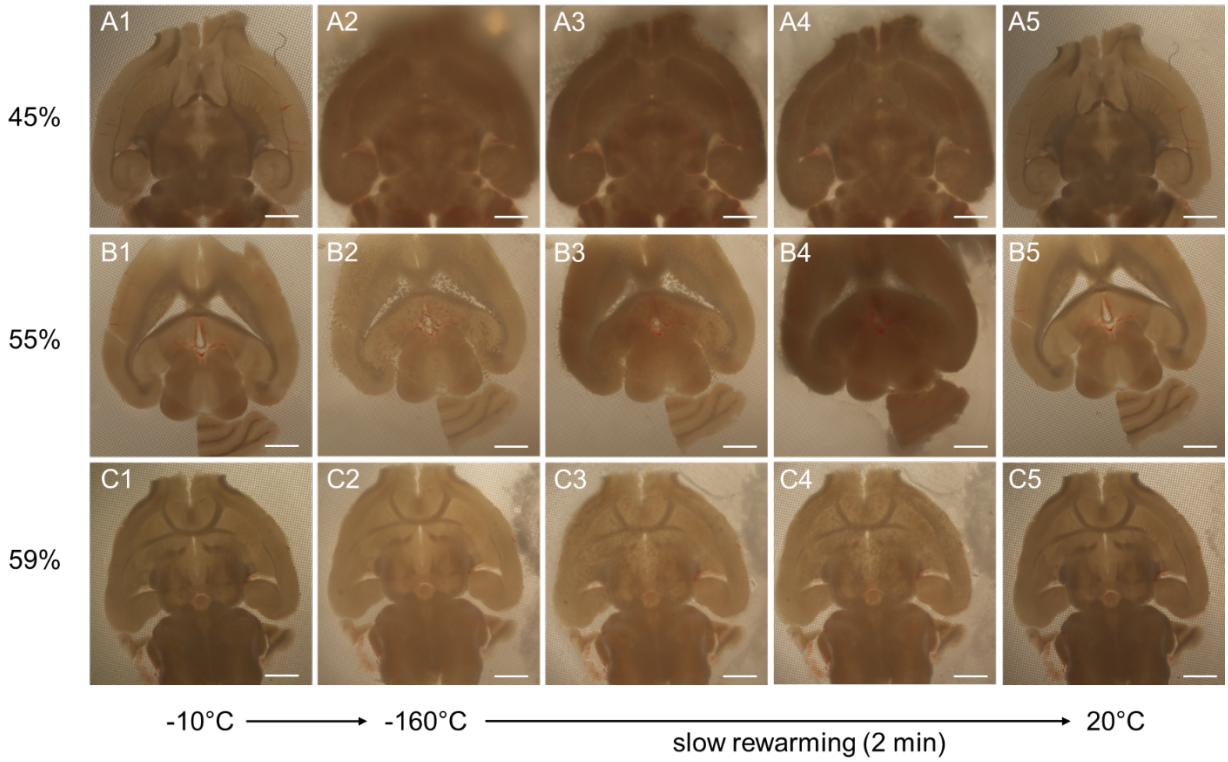

Fig. S3. Cooling and rewarming phase crystallization of brain slices.

Destruction of brain slices due to cooling and rewarming phase crystallization during slow rewarming. Brain slices were incubated at -10 °C for 2h in target concentrations of 45% (**A1**)-(**A5**), 55% (**B1**)-(**B5**), and 59% w/v V3 (**C1**)-(**C5**), followed by brief immersion in 65% w/v V3. (**A1**), (**B1**), (**C1**) show slices at the end of incubation. (**A2**), (**B2**), (**C2**) show slices at cryogenic temperature after cooling on a -196 °C copper cylinder and -160 °C Isopentane covering. (**A2**) shows extensive, (**B2**) slight, (**C2**) no cooling phase crystallization. (**A3**) and (**A4**) show further loss of transparency during rewarming, which returns to baseline transparency after completed rewarming to RT in (**A5**). (**B3**) and (**B4**) show extensive rewarming phase crystallization with loss of transparency, which returns to baseline transparency after rewarming to RT in (**B5**). (**C3**) and (**C4**) show slight rewarming phase crystallization and return to baseline in (**C5**) at RT. Rewarming phase is recorded in Movie S1, S5, S7. Stereo microscopy with -160 °C isopentane covering. Lighting from behind. Image contrast enhanced by 42%. Scale bars 1 mm.

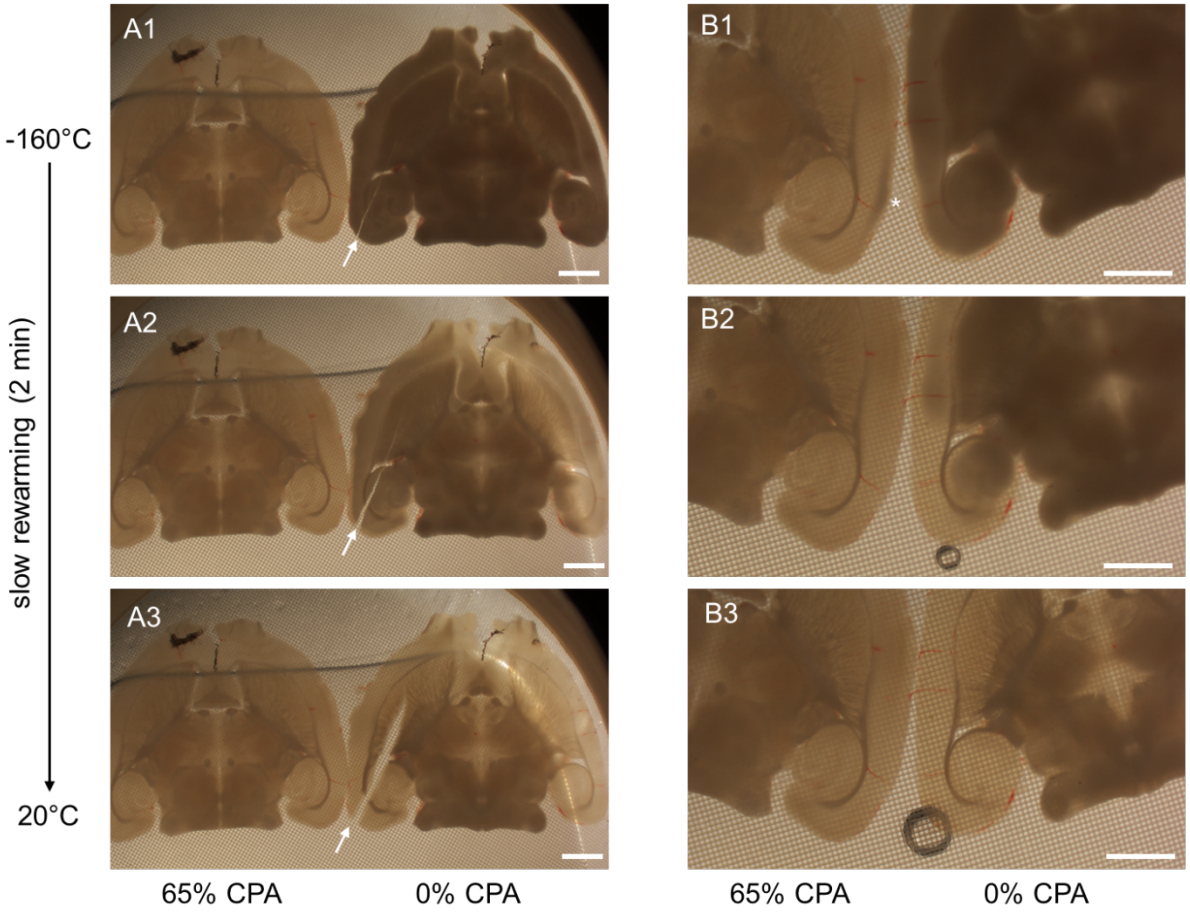

Fig. S4. Stable vitrification vs. crystallization and cracking of brain slices

Comparison of stable vitrification (left) vs. crystallization (right) of brain slices. The left slice was incubated at -10 °C for 2h in a target concentrations of 65% w/v V3, the right slice was incubated in LM5 carrier solution only. (**A1**) and (**B1**) show slices at cryogenic temperature after cooling on a -196 °C copper cylinder and -160 °C Isopentane covering with loss of transparency due to crystallization in the right slice. Transparency returns gradually (**A2**), (**B2**) during rewarming to RT (**A3**), (**B3**), while the vitrified is rewarming without crystallization. (**A1**)-(**A3**) show a crack from thermomechanical stress in the crystallized slice (Arrows). (**B1**) shows crystallization in the vitrified slice due to loss of CPA (asterisk). The rewarming phase is recorded in Movie S12. Stereo microscopy with -160 °C isopentane covering. Lighting from behind. Image contrast enhanced by 42%. Scale bars 1 mm.

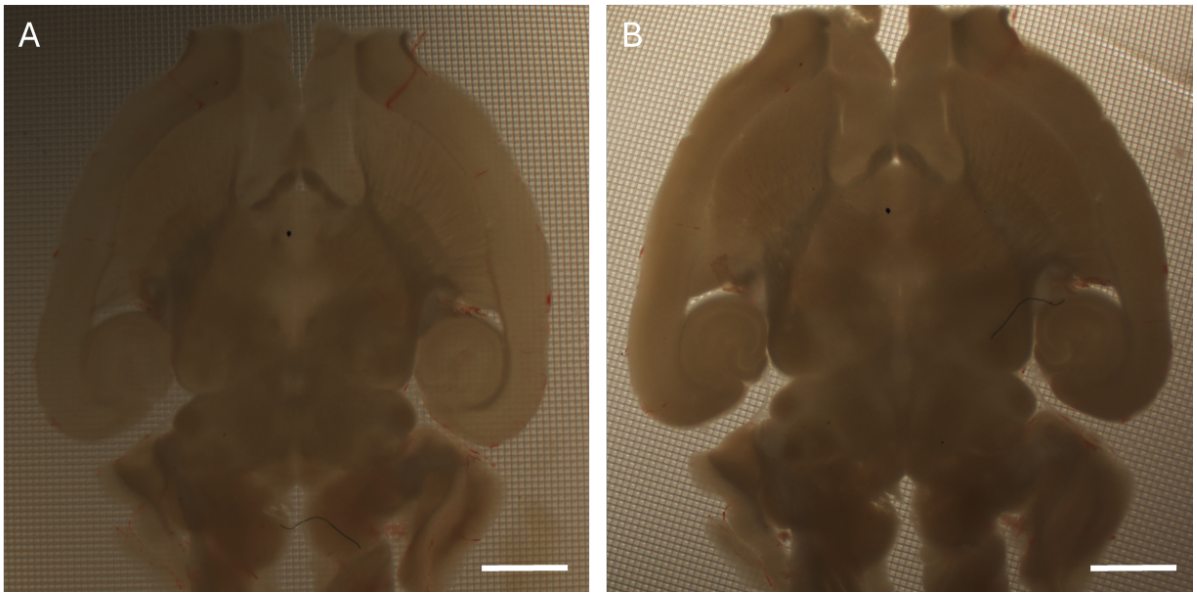

Fig. S5. Swelling and loss of transparency during CPA unloading.

Comparison of the same brain slice during optimized vitrification protocol. (**A**): Slice after incubation step with 59% w/v V3. (**B**): Slice after incubation step with 16% w/v V3 and added mannitol shows loss of transparency and swelling. The area of slice is increased by 8% in (**B**) compared to (**A**). Lighting from behind. Image contrast enhanced by 42%. Scale bars 1 mm.

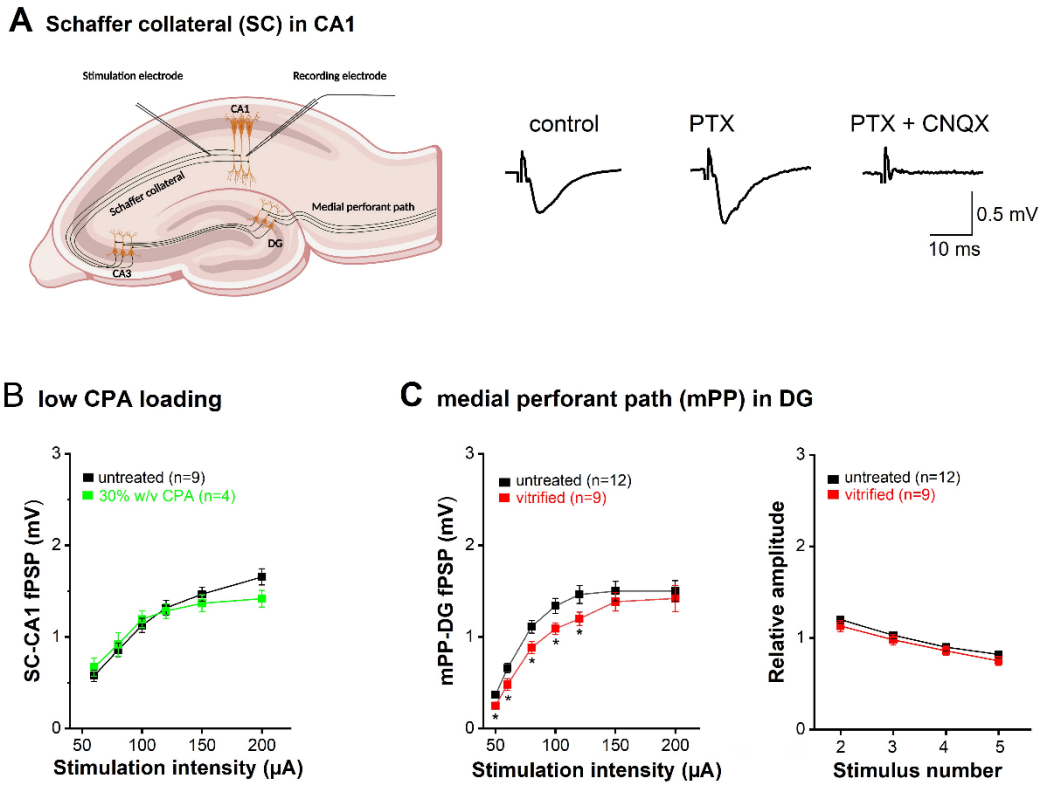

Fig. S6. Properties of synaptic transmission derived from extracellular field recordings in area CA1 and dentate gyrus.

(**A**) Schematic drawing of canonical tri-synaptic circuit within a mouse hippocampal slice showing location of stimulating and recording electrodes to examine fPSPs at the SC-CA1 synapse. Raw voltage traces on the right depict fPSPs from a vitrified slice (10 min at -196 °C and 4 h post rewarming) in normal bath solution (control), in the presence of the $GABA_A$ receptor antagonist picrotoxin (PTX, 100 µM), and in the presence of the AMPA receptor antagonist CNQX (40 µM); stimulus intensity was 70 µA. Drawing was created in BioRender. German, A. (2025) https://BioRender.com/b67t366 (**B**) Effect of CPA loading with 30% w/v on I-O curves from SC-CA1 synapse. (**C**) Downward shift of I-O curve from mPP-GC synapse after vitrification when compared to untreated controls (left panel). In contrast, STP remained unaffected after vitrification (right panel). * $p < 0.05$

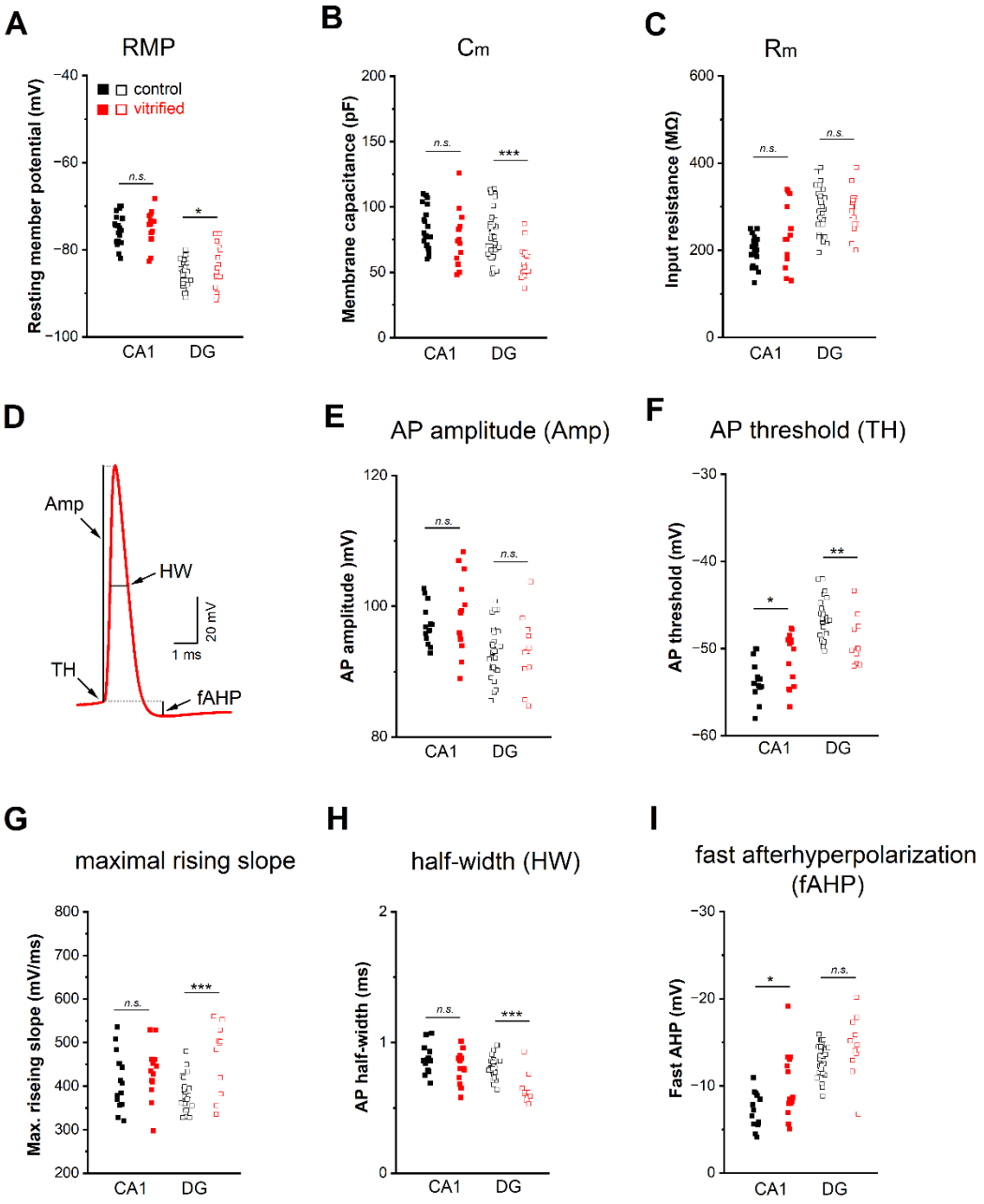

Fig. S7. Passive membrane properties and action potentials in vitrified hippocampal principal cells.

(**A-C**) Summary of resting membrane potential (RMP, **A**), membrane capacitance (C_m, **B**) and input resistance (R_m, **C**) in hippocampal cells from untreated and vitrified slices. (**D**) Single AP waveform from CA1 pyramidal cell from a vitrified slice (1 day at -150 ºC and 6 h post rewarming in normal bath solution) demonstrating how parameters were defined. (**E-I**) Individual data points for peak amplitude (**E**), voltage threshold (**F**), maximum rising slope (**G**), half-width (**H**) and fast afterhyperpolarization (fAHP, **I**) of evoked action potential. Statistical

comparisons were performed using an unpaired, two-tailed t-test. n.s. not significant; * $p < 0.05$; ** $p < 0.01$; *** $p < 0.001$.

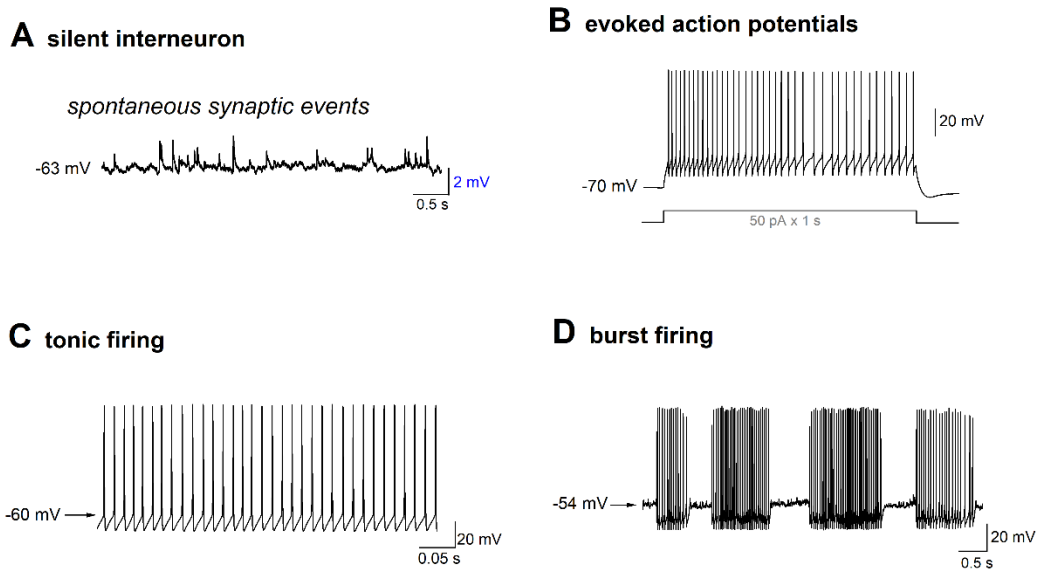

Fig. S8. Evidence for neurophysiologically sound CA1 interneurons after vitrification

Whole-cell current-clamp recordings from interneurons whose somata were located within or next to CA1 pyramidal cell layer, all from vitrified slices. (**A-B**) Silent interneuron receiving spontaneous synaptic input at rest (-63 mV; **A**), and discharging action potentials upon depolarization (50 pA for 1 s; initially held at -70 mV; **B**). (**C-D**) Examples of two electrophysiologically distinct interneurons exhibiting spontaneous action potential firing at rest, either in a tonic fashion (**C**), or in burst-like mode (**D**).

790

Table S1.
Carrier solution LM5.

chemical	concentration
glucose	90 mM
mannitol	45 mM
lactose	45 mM
KCl	8.2 mM
K_2HPO4	7.2 mM
glutathione	5 mM
adenine	1 mM
$NaHCO_3$	10 mM

795

90

Table S2.
Modified standard vitrification solution (59% w/v V3 = 8.42 M permeable CPA).

chemical	concentration
dimethylsulfoxide (DMSO)	22.3% w/v
ethylene glycol (EG)	16.84% w/v
formamide	12.86% w/v
polyvinylpyrrolidone K12	7% w/v

800

805 **Table S3.**

Optimized vitrification protocol.

concentration V3	concentration mannitol	duration	temperature
Slicing in sucrose-aCSF		20 min	4 °C
Incubation in sucrose-aCSF		10 min	35°C
Incubation in aCSF		30 min	20°C
0%	45 mM	2 min	10 °C
2%	45 mM	2 min	10 °C
4%	45 mM	2 min	10 °C
8%	45 mM	2 min	10 °C
16%	45 mM	2 min	10 °C
30%	45 mM	5 min	10 °C
45%	45 mM	2 min	-10 °C
59%	45 mM	5 min	-10 °C
59%	45 mM	5 min	-10 °C
59%	45 mM	5 min	-10 °C
Liquid nitrogen		>10 min	-196 °C
52%	45 mM	20 s	-10 °C
45%	345 mM	2 min	-10 °C
30%	345 mM	5 min	-10 °C
16%	345 mM	10 min	10 °C
8%	345 mM	3 min	10 °C
4%	345 mM	3 min	10 °C
2%	345 mM	3 min	10 °C
0%	345 mM	10 min	10 °C
0%	45 mM	10 min	10 °C
Incubation in aCSF		>30 min	20 °C

Movie S1. Slow rewarming 45%

Slow rewarming of brain slice from fig. S4A after 45% w/v V3 loading. Complete crystallization during cooling phase. Stereo microscopy with -160 °C isopentane covering. Lighting from behind. Mesh size 74 µm.

Movie S2. Slow rewarming 52%

Slow rewarming of brain slice after 52% w/v V3 loading. Near-complete crystallization during cooling phase. Complete crystallization during rewarming phase. Stereo microscopy with -160 °C isopentane covering. Lighting from behind. Mesh size 74 µm.

Movie S3. Slow rewarming 53%

Slow rewarming of brain slice after 53% w/v V3 loading. Partial crystallization during cooling phase. Complete crystallization during rewarming phase. Stereo microscopy with -160 °C isopentane covering. Lighting from behind. Mesh size 74 µm.

Movie S4. Slow rewarming 54%

Slow rewarming of brain slice after 54% w/v V3 loading. Partial crystallization during cooling phase. Complete crystallization during rewarming phase. Stereo microscopy with -160 °C isopentane covering. Lighting from behind. Mesh size 74 µm.

Movie S5. Slow rewarming 55%

Slow rewarming of brain slice from fig. S4B after 55% w/v V3 loading. Partial crystallization during cooling phase. Complete crystallization during rewarming phase. Stereo microscopy with -160 °C isopentane covering. Lighting from behind. Mesh size 74 µm.

Movie S6. Slow rewarming 56%

Slow rewarming of brain slice after 56% w/v V3 loading. Partial crystallization during cooling phase. Complete crystallization during rewarming phase. Stereo microscopy with -160 °C isopentane covering. Lighting from behind. Mesh size 74 µm.

Movie S7. Slow rewarming 59%

Slow rewarming of brain slice from fig. S4C after 59% w/v V3 loading. Partial crystallization during rewarming phase. Stereo microscopy with -160 °C isopentane covering. Lighting from behind. Mesh size 74 µm.

Movie S8. Rapid rewarming 56%

Rapid rewarming of brain slice after 56% w/v V3 loading by covering with 52% w/v V3 solution at -10 °C. Obvious crystallization from cooling phase. Stereo microscopy. Lighting from behind. Mesh size 74 µm.

Movie S9. Rapid rewarming 57%

Rapid rewarming of brain slice after 57% w/v V3 loading by covering with 52% w/v V3 solution at -10 °C. Slight crystallization from cooling phase. Stereo microscopy. Lighting from behind. Mesh size 74 µm.

Movie S10. Rapid rewarming 58%

Rapid rewarming of brain slice after 58% w/v V3 loading by covering with 65% w/v V3 solution at -10 °C. No crystallization from cooling phase. Stereo microscopy. Lighting from behind. Mesh size 74 µm.

850 **Movie S11. Rapid rewarming 59%**

Rapid rewarming of brain slice after 59% w/v V3 loading by covering with 65% w/v V3 solution at -10 °C. No crystallization from cooling phase. Stereo microscopy. Lighting from behind. Mesh size 74 µm.

Movie S12. Slow rewarming 65% vs 0%

855 Slow rewarming of brain slices from fig. S5A after 65% w/v V3 loading (left) and 0% loading (right). No evidence for rewarming phase crystallization in the vitrified slice. Stereo microscopy with -160 °C isopentane covering. Lighting from behind. Mesh size 74 µm.

860